Title
Atomic Structure of Surface-Densified Phases in Ni-Rich Layered Compounds

Permalink
https://escholarship.org/uc/item/7z32z41n

Journal
ACS Applied Materials & Interfaces, 13(15)

ISSN
1944-8244

Authors
Mukherjee, Pinaki
Lu, Ping
Faenza, Nicholas
et al.

Publication Date
2021-04-21

DOI
10.1021/acsami.1c00143

Peer reviewed

Atomic Structure of Surface Densified Phases in Ni-Rich Layered Compounds

P. Mukherjee[1], P. Lu[2], N. Faenza[3], N. Pereira[3], G.G. Amatucci[3], G. Ceder[4,5] and F. Cosandey[6]

[1]Materials Science and Engineering, Michigan Technological University, Michigan 49931, United States.
[2]Sandia National Laboratories, Albuquerque, New Mexico 87185, United States.
[3]Energy Storage Research Group, Rutgers University, New Jersey 08902, United States.
[4]Materials Science and Engineering, University of California, Berkeley, California 94720, United States.
[5]Materials Science Division, Lawrence Berkeley National Laboratory, California 94720, United States.
[6]Materials Science and Engineering, Rutgers University, New Jersey 08854, United States.

Corresponding Authors:

Pinaki Mukherjee <grad.pinaki@gmail.com>

Frederic Cosandey <fred.cosandey@gmail.com>

Abstract

In this work, we report the existence of surface densified phases (β-Ni_5O_8, γ-Ni_3O_4, and δ-Ni_7O_8) in $LiNiO_2$ (LNO) and $LiNi_{0.8}Al_{0.2}O_2$ (LNA) layered compounds by combined atomic level scanning transmission electron microscopy (STEM) and electron energy loss spectroscopy (EELS). These surface phases form upon electrochemical aging at high state of charge corresponding to a fully delithiated state. A unique feature of these phases is the periodic occupancy by Ni^{2+} in the Li layer. This periodic Ni occupancy gives rise to extra diffraction reflections, which are qualitatively similar to those of the $LiNi_2O_4$ spinel structure, but these surface phases have a lower Ni valence state and cation content than spinel. These experimental results confirm the existence of thermodynamically stable surface phases and provide new insights into the phenomena of surface phase formation in Ni-rich layered structures.

Introduction

Ni-rich layered oxides such as $LiNi_{0.8}Co_{0.15}Al_{0.05}O_2$ (NCA) or $LiNi_{0.8}Co_{0.1}Mn_{0.1}O_2$ (NCM811) are among the highest capacity cathode materials used commercially[1-3]. However, at the highest state of charge (fully delithiated state) these cathode materials suffer capacity loss and impedance rise caused primarily by the formation of surface phases[4-5]. Our present understanding on the formation of surface phases is as follows: first surface oxygen vacancies are created from reaction with the electrolyte followed by reduction of transition metal ions and inward migration of mobile Ni^{2+} transition metal ion[6-7]. This leads to the formation of a few nanometer thick dense surface phase with rocksalt ($Fm\bar{3}m$) structure at the surface and a layered ($R\bar{3}m$) phase in the interior with partial Ni^{2+} filling of the Li layer[4, 8-11].

This phase transformation from layered at the interior to the rocksalt phase at the surface is sometime mediated by the formation of a spinel-like intermediate phase at the sub-surface[10, 12-15]. The terminology “spinel-like” or “disordered spinel” has been introduced in the literature as these cation-mixed phases show extra diffraction reflections similar to those of spinel but do not show images with all the symmetry elements of the spinel ($Fd\bar{3}m$) structure. In most studies, phase identification was obtained by observing extra reflections in digital diffractograms (also known as Fast Fourier transform (FFT)) of high-resolution lattice images, which only show that a periodicity corresponding to spinel is present in the high-resolution images. Only in a few studies for Mn-rich layered compounds, precise images by atomic resolution high angular dark field scanning transmission electron microscopy (HAADF-STEM) unambiguously reveal the contrast of a spinel phase[16-18]. In $LiCoO_2$, a Co_3O_4 spinel phase can also form readily at the surface[19]. In contrast to Mn-rich or Co-rich layered compounds, spinel formation in Ni-rich layered materials is less likely to occur due to much slower kinetics[20].

In Ni-rich compounds, bulk transformation from layered to spinel has been observed primarily during high temperature stability studies above 150°C accompanied by oxygen loss [14, 21-25]. At the normal operating temperature of Li-ion batteries, $LiNi_2O_4$ spinel phase is not likely to occur. In addition, surface phases are generally formed in a reduced environment triggered by oxygen loss where Ni will have a lower valence state than that of spinel. This has led to an investigation by first principle methods to determine if other stable phases could be present in the $LiNiO_2$-NiO_2-NiO ternary phase diagram[26]. As described in detail in the next background section, three new equilibrium stable phases have indeed been found in the ternary phase diagram with composition between the delithiated layered α-NiO_2 and NiO. These phases have similar diffraction characteristics to spinel but with reduced Ni valence state and oxygen content.

A complete experimental identification of these phases requires a combination of atomistic visualization of the structure with quantitative determination of Ni/O ratio as well as Ni valence state. In this work, we have searched for these existence of surface densified phases by direct atomic scale imaging using aberration corrected scanning transmission electron microscopy (AC-STEM) and electron energy loss spectroscopy (EELS) experiments on two Ni-rich model systems, $LiNiO_2$ (LNO) and Al-substituted $LiNi_{0.8}Al_{0.2}O_2$ (LNA), to determine the atomic structure, chemistry and Ni valence state of the surface phases. We have synthesized near-stoichiometric LNO as a model system to draw one to one correspondence between the theoretical predictions and experimental studies. We performed STEM/EELS experiments on these two cathode materials that were first charged (fully delithiated) at 4.75V for two weeks followed by discharged (re-lithiated) at 2.7V. Further detailed information on material synthesis and electrochemical performance of LNO and LNA at 4.75V can be found in a companion paper [27]

Background

The Ni-Li-O ternary phase diagram was recently computed using first-principle simulation-based techniques [26] which is reproduced schematically in the Figure 1. The three vertices of the triangle are formed by the layered $LiNi^{3+}O_2$, space group $R\bar{3}m$ (marked as L), the delithiated layered $Ni^{4+}O_2$, space group c2/m (marked as α) and the rocksalt $Ni^{2+}O$, space group $Fm\bar{3}m$ (marked as R) phases. The side joining the L and the α phase is the Li concentration axis, as the L to α phase transition occurs by delithiation. The spinel phase $LiNi_2O_4$ (marked as S) occurs at the middle of this axis and is stable for a narrow Li and O concentration range with a $Ni^{3.5+}$ valence state. The side joining the R and the L phase is the Ni concentration axis while the side joining the α and the R phases is the vacancy concentration or oxygen loss axis.

In addition to these corner phases, the simulations predict the stable formation of three new phases along the oxygen loss path between α-NiO_2 and R-NiO. These phases are β-$Ni_{1.25}O_2$ space group ($R\bar{3}m$), γ-$Ni_{1.5}O_2$ space group (Cmmm) and δ-$Ni_{1.75}O_2$ space group ($Fm\bar{3}m$). The crystal structures of the β, γ, and δ projected along equivalent $[110]_L$ (equivalent zone axis of layered structure) altogether with α, R, and spinel phases are presented in Figures 2a through 2f. The $[110]_L$ zone axis is crucial to understand the structure of these phases as, in this direction, they are viewing directly along the Ni (3a) and Li (3b) layers. Along this zone axis, we can clearly see the Li layer of the parent layered structure ($R\bar{3}m$) and its subsequent ordered filling with Ni^{2+} in the β, γ and δ phases. The top row in Figures 2a to 2e show that the original Li 3b layer is progressively occupied by more Ni^{2+} cations as we move from the α to the R phase with a corresponding decrease in average Ni valence state from 4+ in α-NiO_2 to 3.2+, 2.66+ and 2.28+ for β, γ and δ phases respectively. In addition, the Ni over O ratio is observed to increase with Ni/O ratio corresponding to 0.65, 0.75 and 0.875 for β, γ and δ respectively, reflecting the densification of the structures. Furthermore, the gradual filling of Li layer by Ni^{2+} is not random but ordered on alternate Li vacant sites. In the β phase, the sites are alternatively empty, or half-occupied; in the γ phase, the sites are alternatively empty or fully occupied while in the δ phase the sites are alternatively half-empty or fully occupied.

Although the crystal structures and chemistry corresponding to these phases are unique, their diffraction patterns are qualitatively quite similar to that of spinel[20]. The simulated kinematic diffraction patterns of the α, β, γ, δ and R phases viewed along $[110]_L$ or $[110]_{R,S}$ zone axis are presented in the middle row of Figures 2a through 2e along with the diffraction pattern of the spinel phase (S) in Figure 2f. It can be observed that this periodic ordering of Ni^{2+} in the Li layer of the β, γ, δ phases gives rise to extra reflections which are qualitatively the same as the reflections from the spinel phase. The only difference is the absence of {200} kinematically forbidden reflections in the spinel structure which are marked by dotted circles. In practice however, theses reflections often appear because of dynamical plural scattering sometime referred to as double diffraction. Therefore, it is not possible to distinguish between these phases based solely on diffraction. The dynamical scattering also washes out the relative variations in intensities and it is with only quantitative kinematical diffraction analysis that the crystal structures of these phases can be determined.

These phases, however, are quite distinct in terms of their atomic structure, Ni valence and Ni/O concentration ratio. It is only through a combination of imaging and spectroscopy techniques that these new phases can be identified. The bottom row of Figures 2a to 2e show the HAADF-STEM image simulations of the various phases from layered α-NiO_2 to dense rocksalt R-NiO. The bottom row of Figure 2f shows the image simulation for $LiNi_2O_4$ spinel. The common feature of the three new phases β-Ni_5O_8, γ-Ni_3O_4 and δ-Ni_7O_8 is the ordered filling of the Li (3b) layer by Ni^{2+}, which occurs on alternate Li sites.

In HAADF-STEM imaging mode, the atomic image contrast is proportional to $Z^{2-\delta}$ with the factor δ dependent on microscope parameters such as the inner and the outer diameters of the dark field detector[28-29]. The scattering from O or Li are too weak to be detected and the Li layer appears black regardless of the Li content, and the bright contrast is directly proportional to the number of Ni atoms in a column. For β-Ni_5O_8, the alternate contrast in the Li (3b) layer is half that of the Ni (3a) layer while for γ-Ni_3O_4 all the atomic columns have the same intensity with alternate unoccupied site along the Li layer. For δ-Ni_7O_8, the vacant site is now half occupied with half the intensity on alternate site while for R-NiO all the sites are equally occupied and have the same intensity. In the $LiNi_2O_4$ spinel structure phase however, the image contrast along $[110]_S$ is quite different with ordering of Ni atoms on two different {111} planes as shown schematically in the top row of Figure 2f with the corresponding image simulation shown in the bottom row. Along this $[110]_S$ viewing direction, the Ni atomic columns in the original Li layer are empty and half occupied giving rise to a periodic contrast similar to β-Ni_5O_8 in the equivalent Li layer. Importantly, in the spinel phase there is a periodic contrast in the Ni layer as well. This is quite different from the three new phases, which show a uniform contrast along the Ni layer. Therefore, imaging by HAADF-STEM can unambiguously distinguish the various phases.

RESULTS

We have used atomic resolution HAADF/STEM imaging with quantitative EELS analysis to search for the presence of the cation-ordered phases on two cathode chemistries, $LiNiO_2$ (LNO) and $LiNi_{0.8}Al_{0.2}O_2$ (LNA), which were delithiated at 4.75 V for two weeks followed by re-lithiation at 2.75 V. The cathode materials were synthesized in the laboratory using standard methods resulting in the formation of nanoparticles with average size of 450 nm[27]. A small fraction of the particles had a plate-like shape with about 5-20 nm in thickness with well-defined facets. A low magnification image of the particles and a representative image of such a plate-like particle are shown in Figure S1 (a, b). In this TEM study, we have used these faceted particles, as they are easier to detect and have an average thickness suitable for atomic scale imaging over large distances.

STEM and EELS Analysis of $LiNiO_2$ (LNO) Samples

The HAADF STEM image of an area at the edge of a particle in LNO oriented along the $[110]_L$ zone axis is shown in Figure 3a. Due to the weak atomic scattering of Li and O, only Ni atoms are imaged by HAADF-STEM. At the edge of the particle, the atomic contrast corresponds to the R-NiO structure. The contrast gradually changes to a more layered contrast with alternate bright and weaker dots parallel to the edge revealing the original Ni (3a) sites and Ni partially occupying the Li (3b) sites. Figures 3 b-d shows magnified images from three regions of the particle about 6 nm apart from each other. Figures 3 e-g shows the corresponding FFTs from these three regions. The FFTs reveal a gradual development of extra reflections, which are marked by red arrows. Near the edge (Figure 3g) these reflections are missing and the FFT consists of the superposition of $R\bar{3}m$ layered and $Fm\bar{3}m$ rocksalt reflections. These extra reflections start to appear around 9 nm from the edge and become stronger with the appearance of two more extra reflections further in the interior (Figure 3e). These extra reflections form a diffraction pattern which is identical to one of the new β, γ or δ phases (Figures 2 b-d second row). The corresponding HAADF-STEM image is enlarged in Figure 3h showing a regular layered structure with Li sites occupied by Ni but the filling is not random but in places has double periodicity. The image intensity profile along the Ni layer (blue line) and the Li layer (green line) are shown in Figure 3i and 3j respectively. The profile corresponding to the blue line (Figure 3i) is almost constant, but the profile corresponding to the green line (Figure 3j) has intensity variations indicative of periodic distribution of Ni with double periodicity. This double periodic contrast give rise to the extra reflections observed in the FFT. The average intensity variation is about 0.6 with a range of 0.5-0.8. The line profile across the Ni and Li layers (Figure S2) shows two values for Li/Ni for the two-site occupancy corresponding to 0.53 and 0.35. The presence of a contrast with double periodicity in the Li (3b) sites but not in the Ni (3a) sites indicates the presence of one of the densified surface phases (Figure 2 third row). As the sites in the Li layer are all partially occupied by Ni, the phase closely matches that of δ-Ni_7O_8 (Figure 2d). A simulated HAADF image of the δ-Ni_7O_8 phase is overlaid as insert in Figure 3h.

The typical EELS data of Li-K, Ni-M, O-K and Ni-L edges obtained from the same area are presented in Figure S3. The oxygen edge is composed of a main peak and a smaller pre-peak about 12.4 eV lower than main peak (Figure S3 (b)). This pre-peak occurs from an electron transition from O1s to hybridized O2p-Ni3d orbitals[30]. The intensity as well as the position of the pre-peak decrease with a reduction of oxygen content and the variation of the valence state of the transition metal associated with oxygen (Figure S3 (b)). The evolution of oxygen pre-peak position and relative height as a function of distance from the surface are presented in Figure S4a. A decrease in the O-K pre-peak height and position are detected indicative of a nickel reduction at the surface consistent with the presence of a cubic R-NiO phase at the surface. The valence of Ni has been quantified using the Ni-L_3/L_2 ratio technique[31]. There is a large scatter of the Ni valence and Ni/O atomic ratio as a function of distance but average values of Ni valence of 2.8 (±0.4) and atomic Ni/O of 0.59 (±0.1) are also indicative of a reduced surface compared to delithiated layered α-$Ni^{4+}O_2$. We did not attempt to quantify the amount of Li, but the presence of a Li-K edge indicates the presence of Li at the near surface region (Figure S3 (a)). From the experimental Ni valence and Ni/O ratio data obtained by EELS, this phase is closer to the γ-Ni_3O_4 phase (Figure 2c).

STEM and EELS Analysis of $LiNi_{0.8}Al_{0.2}O_2$ (LNA) Samples

The HAADF STEM image of a LNA particle is depicted in figure 4a with a magnified atomic resolution image from ROI 1 shown in Figure 4b. The lower right corner marked in red is further magnified in Figure 4c revealing the presence of Ni in the Li layer with double periodicity. The corresponding FFT shown in Figure 4d, reveal the presence of extra reflections (marked by red arrows). These extra reflections form a pattern, which is similar to one of the new phases (Figure 2 b-d, second row). Two interesting things to note here are that the features typical of one of the phases is confined to a very small area of approximately 10 nm^2 and that the change from the layered to the new structure is continuous. Figure 4c shows a magnified view of the HAADF-STEM image with the intensity profile along the Ni layer (blue line) and along the Li layer (green line) in Figures 4e and 4f respectively. The intensity profile in the Li layer has a double periodicity typical of one of the new phases (Figure 2). The line profile across the Ni and Li sites shows that the Li/Ni (Figure S5) intensity ratio is 0.25. The image contrast with double periodicity is closely related to the β-Ni_5O_8 phase with Li sites alternatively empty or half-occupied (Figure 2b bottom row). A simulated HAADF image of the β-Ni_5O_8 phase is overlaid as insert in Figure 4c.

The typical EELS Li-K, Ni-M, O-K, Ni-L and Al-K edges taken from the same area are presented in Figure S6 with in Figure S7 the corresponding EELS data taken as a function of distance from the edge. The results are qualitatively similar to those observed in LNO (Figure S4) with a decrease of O pre-peak intensity and position in the first 3nm from the particle edge. The Ni/O ratio is also lower reflecting cationic densification at the surface. The average values of Ni valence and Ni/O atomic ratio are 2.9 (±0.1) and 0.57 (±0.1), respectively. Al is also present at the surface as shown in Figure S6 (d) but quantification of the Al content is difficult due to the low Al signal intensity. However, assuming complete substitution of Al (20%) in the Ni site as measured experimentally by atomic resolution EDS [32], a corrected (Ni+Al)/O ratio of 0.71 is obtained which with $Ni^{+2.9}$ are closely related to the γ-Ni_3O_4 phase.

The Al distribution in the plate-like particles was quite inhomogeneous with resulting local variations in crystal structures including layered, spinel-like and rocksalt phases (Figure S8 and S9). In general, the layered structure was found predominantly in Al- rich areas indicating that Al can help in stabilizing the layered structure [24, 27]. Figure 5a shows a high magnification HAADF-

STEM image of the interface region between layered and rocksalt structures (For a low magnification image see Figure S9 (c)). The structure varies from layered (upper-left corner) to rocksalt (lower right corner). This interface is similar to the one simulated recently consisting of a NiO source embedded in a layered structure[20]. The corresponding FFT are shown in Figure 5b and 5d respectively with an intermediate pattern (Figure 5c) at the interface showing extra reflections typical of one of the densified phases. The magnified Fourier filtered images are depicted in Figures 5 e-g. In the layered structure (Figure 5e), a uniform weak atomic contrast is visible in the Li layer revealing the presence of Ni while in the interfacial region the contrast shows an alternative bright and less bright variation on Li sites, indicating different occupancies of Ni atoms at those sites with double periodicity. The STEM contrast of this area is somewhat in between δ-Ni_7O_8 and γ-Ni_3O_4 (Cmmm) phase with alternative Li sites which are fully or partially occupied, respectively. In the computer simulation studies, the interface region between rocksalt and layered was found to be predominantly the γ-Ni_3O_4 phase with β-Ni_5O_8 further away from the interface[20].

Discussion

The results of this investigation confirm the presence of surface densified phases characterized by the presence of a periodic and ordered Ni^{2+} occupation of the Li layer. The phases exist at the surface of electrochemically aged LNO and LNA and at the interface between rocksalt and layered phases in LNA. We have not found any of these phases in the pristine samples that we have characterized. To reduce the effect of beam damage, especially during EELS measurements, we have used spot size 9 and longer areas (approximately 2 nm × 20 nm) along the edge of the sample. Electron beam damage does not usually form an ordered structure, rather it produces disordered rocksalt structures. Figure S10 shows a beam-damaged area before and after EELS acquisition. It does not show any change in the original STEM contrast. A necessary condition for the formation of these phases is the availability of mobile Ni^{2+} ions, which form due to cathode electrolyte reactions at high state of charge. A complete agreement between HAADF-STEM images and chemistry is not obtained but our combined results point toward the unambiguous observation of densified phases at the surface of Ni-rich layered compounds as predicted theoretically [26]. The presence of Ni cation ordering, however, is not commonly observed compared to images where the occupancy of Ni in Li (3b) sites is random. In our previous investigations[10] as well as others [9, 11], a gradual filling of the Li (3b) sites is observed with at times complete disordering with the presence of cubic rocksalt type phase[10, 33]. One possibility of this low occurrence is the improper choice of the viewing orientation. In the case of γ-Ni_3O_4 phase the two zone axis $[110]_L$ and $[010]_L$ are not equivalent, while they are equivalent in all other phases. Along the $[110]_L$ zone axis, the periodic Ni cation filling is visible but viewed along the $[010]_L$ the ordering is not visible with the Li layer in average half occupied by Ni. It is therefore possible that this phase can be missed if not viewed along the proper zone axis[20]. Another consideration is the mechanism and driving force for cation ordering. Zou et.al.[33] studied surface phase formation in $LiNi_{0.76}Mn_{0.14}Co_{0.1}O_2$ (NMC) and propose that the driving force for surface formation is dependent on the rate and depth of charge. In their study, an intermediate phase with periodic contrast in the Li layer was found only for high rate of charge but a disordered rocksalt was found at low rate of charge. In case of a slow charging, almost all of Li^+ ions are extracted and Ni^{2+} ions occupy all the vacant Li sites randomly. During fast charging some Li^+ remains in the layered structure, that Ni^{2+}ions cannot occupy. Ni^{2+} ions then occupy alternate sites to form a phase with similar periodic contrast as the densified phases presented here[33]. In their study, the periodic filling of Li layer by Ni^{2+} ions is interpreted as an incomplete transformation from layered to spinel[33]. Similarly, in a $LiNi_{0.495}Mn_{0.495}Mo_{0.01}$ (LNMMO) layered compound, a subsurface reconstruction is observed in some areas involving a small fraction of cation migration to the Li layer[34]. The reported annular bright field (ABF) STEM image reveals double periodicity along the Li layer with contrast similar to the new phases presented here. The Ni content of this phase is higher than in the bulk and has a Ni^{2+} valence state. This local reconstruction was described as an “incipient-spinel” as it is assumed that this phase is an incipient state between a layer to spinel phase transformation.

All the new phases described here have Ni/O value of approximately 0.6, which lies within the anticipated value of 0.5-0.75 (Figure 1) with a Ni valence state of 2.9 which is much lower than the value of 3.5 for $LiNi_2O_4$ spinel. The results of this investigation as well as those from a computer simulation[20] points towards the stable formation of β-Ni_5O_8 and γ-Ni_3O_4 phases or a combination of the two. In view of the reducing environment with lower oxygen content at the surface and with low average Ni valence state than in spinel, it is not likely that that these densified phases will transform further to a spinel phase. Therefore, we view the presence of these surface densified phases as their final equilibrium state.

From an electrochemical viewpoint, the presence of surface densified phases is detrimental to transport properties as they impede Li diffusion and can give rise to large impedance rise [5, 10]. A detailed knowledge of the structure of surface densified phases allow a more precise modeling of transport kinetics. The surface densified phases described in this study are expected to behave differently as both β-Ni_5O_8 and γ-Ni_3O_4 phases have open channels along equivalent $[110]_L$ direction (Figure 2), while in the δ-Ni_7O_8 phase, these open channels are now occupied by Ni atoms preventing fast diffusion of Li.

Conclusions

In this study, we have confirmed, using combined techniques of atomic scale imaging (HAADF-STEM) and chemical analysis (EELS), the presence of β-Ni_5O_8 and γ-Ni_3O_4 surface densified phases in Ni-rich layered structures predicted by first principle simulations. These phases are formed because of O loss from the surface followed by an inward diffusion of Ni^{2+} ions and ordering along the Li layer. In some cases, we have observed a gradual filling of the Li layer with a continuous contrast from rocksalt to layered structures. Nevertheless, we have observed contrast resulting from Ni^{2+} ordering in three different samples across two different cathode systems, LNO and LNA. These experimental results confirm the existence of thermodynamically stable surface phases and provide new insights into the phenomena of surface phase formation in Ni-rich layered structures.

Experimental Methods

Material Synthesis. The LNO and LNA samples were synthesized at Rutgers University in the Energy Storage Research Group using standard synthesis method for layered compounds[27]. Lithium acetate (Aldrich), aluminum acetate basic hydrate (Alfa Aesar), nickel (II) acetate tetrahydrate (Aldrich), and cobalt (II) acetate (Aldrich) were mixed in stoichiometric amounts based on the precursors' metal content and dissolved in deionized water. While continuously stirring, the water was boiled off and the resulting material was dried for at least 16 hours at 60^{o}C in a dry room (dew point of -35 to -40^{o}C), and then ground into a fine powder with a mortar and pestle. Mixtures were then annealed at 750^{o}C for 4 hours and cooled gradually to room temperature, all in a flowing O_2 gas environment. These annealing temperatures were experimentally identified to produce the highest quality layered structures with respect to phase purity and cation ordering. Post-annealed materials were quickly transferred into the dry room, where they were ground with a mortar and pestle, and then annealed a second time, using conditions identical to the first, before being ground again. To protect the phase purity and surface structure of these layered oxide materials, which has been shown to degrade upon exposure to ambient air, all materials were stored in a dry room (dew point of -35 to -40^{o}C) or Ar-filled glove box (< 0.1 ppm of H_2O and O_2).

Electrochemistry. LNO and LNA tape electrodes were fabricated using the Bellcore method[35]. Casting slurries were a mixture of poly (vinylidene fluoride-co-hexafluoropropylene) (PVDF-HFP, Kynar 2801, Elf Atochem), carbon black (Super P (SP), MMM), propylene carbonate (Aldrich), and acetone (Aldrich). Homogenous slurries were cast, allowed to air dry, and then the propylene carbonate plasticizer was extracted by soaking the tape in anhydrous diethyl ether (Aldrich). All electrodes were dried at 120^{o}C under vacuum for a minimum of 10 hours and stored in an Ar-filled glovebox to avoid atmospheric exposure. All materials evaluated by microscopy were tested in powder form without PVDF-HFP binder to eliminate any possible chemical reactions and signal interference during TEM observations. The LNO or LNA and carbon black materials were dried under vacuum at 100^{o}C for two hours and at 120^{o}C overnight, respectively prior to mixing in an argon-filled glove box using a mortar and pestle. Mixtures encompassed 97.5 wt% LNO or LNA and 2.5 wt.% SP.

Electrochemical tests were performed versus lithium metal in 2032-coin cells (Hohsen) using Celgard and glass fiber separators soaked with 1M $LiPF_6$ in ethyl carbonate (EC): dimethyl carbonate (DMC) at 50:50 in vol.% electrolyte (BASF). Cycling was conducted using a VMP3 (Biologic) or a Maccor battery cycling system. The cells were typically charged at 10 mA/g, up to a cut-off voltage of 4.75 V, held at constant voltage for 2 weeks, then discharged to 2.7 V, all at 24°C. Further information on electrochemical performance of LNO and LNA at 4.75 V can be found in a companion paper [27].

Transmission Electron Microscopy. After electrochemical testing, the cathode materials were extracted from the powder coin cell. These binder-free LNO and LNA powders were then ground in dimethyl carbonate solution using a mortar and pestle in a glove box with Ar atmosphere. The O_2 and H_2O level in the chamber were both below 0.5 ppm. These powders comprise agglomerates of primary particles that are too thick to be electron transparent. Very low energy grinding was necessary to break up the particle agglomerates without destroying the surface structures. The ground powders were suspended in DMC and drop cast onto 200 mesh holey C grids. The HAADF STEM imaging and EELS experiments were performed using a field emission aberration corrected FEI Titan STEM operated at 300 kV (commonly known as TEAM I) at National Center for Electron Microscopy at Lawrence Berkeley National Laboratory. The spatial resolution of the HAADF-STEM system was 0.07 nm. The EELS experiments were conducted with a Gatan Tridiem spectrometer with an energy resolution of 0.8 eV. The convergence and collection semi angle of the EELS detector were 17 mrad and 23 mrad, respectively. The data were analyzed using Gatan Digital Micrograph. In order to minimize electron beam damage, the EELS data were collected by scanning the beam over an area 2 × 20 nm with a total dose of 4.7×10^7 e^-/nm^2. No measurable changes in HAADF STEM images were observed after EELS acquisition.

Additional HAADF-STEM imaging experiments were performed at Sandia National Laboratory on a FEI Titan G2 80-200 STEM with a Cs probe corrector. This TEM is equipped with a quad X-ray energy dispersive (EDS) detector. The spatial resolution of the STEM system was 0.07 nm.

We have used JEMS software for HAADF-STEM simulations. The aberration parameters from the microscope were used for the simulation using the multislice formalism with the frozen lattice approximation and 10 to 20 phonon configurations.

For quantitative analysis of the Ni valence state by EELS, we have used the white line L_3/L_2 edge intensity ratio method[30-31, 36] which was calibrated using standards compounds ($Ni^{+2}O$ and $LiNi^{3+}O_2$ and $LiNi^{3+}_{0.8}Co_{0.15}Al_{0.05}O_2$). Quantitative analysis of the Ni/O atomic ratio by EELS was done using the edge ratio technique and calculated ionization cross-sections using Gatan software. A small correction factor to the calculated cross-sections was introduced based upon quantification measurements against known standards

Acknowledgments

Funding for this work is provided by NECCESS, an Energy Frontier Research Center funded by the U.S. Department of Energy, Office of Basic Energy Sciences under Award Number DE-SC0012583. Work at the Molecular Foundry was supported by the Office of Science, Office of Basic Energy Sciences, of the U.S. Department of Energy under Contract No. DE-AC02-05CH11231. A part of the electron microscopy research was performed at the Applied Chemical and Morphological Analysis Laboratory (ACMAL) at Michigan Technological University. The ACMAL electron microscopy facility is supported by NSF MRI 1429232. Sandia National Laboratories is a multi-program laboratory managed and operated by National Technology and Engineering Solutions of Sandia, LLC., a wholly owned subsidiary of Honeywell International, Inc., for the U.S. Department of Energy's National Nuclear Security Administration under contract DE-NA0003525. This paper describes objective technical results and analysis. Any subjective views or opinions that might be expressed in the paper do not necessarily represent the views of the U.S. Department of Energy or the United States Government. Special thanks to Prof. Pierre Stadelmann for helpful discussions regarding HAADF-STEM image simulations.

References

1. Liang, L. Z., W.; Zhao, F.; Denis, D. K.; Zaman, F. u.; Hou, L.; Yuan, C., Surface/Interface Structure Degradation of Ni-Rich Layered Oxide Cathodes toward Lithium-Ion Batteries: Fundamental Mechanisms and Remedying Strategies. . *Advanced Materials Interfaces* **2020,** *7* (3), 1901749.
2. Manthiram, A.; Song, B. H.; Li, W. D., A perspective on nickel-rich layered oxide cathodes for lithium-ion batteries. *Energy Storage Mater* **2017,** *6*, 125-139.
3. Myung, S. T.; Maglia, F.; Park, K. J.; Yoon, C. S.; Lamp, P.; Kim, S. J.; Sun, Y. K., Nickel-Rich Layered Cathode Materials for Automotive Lithium-Ion Batteries: Achievements and Perspectives. *Acs Energy Lett* **2017,** *2* (1), 196-223.
4. Hayashi, T.; Okada, J.; Toda, E.; Kuzuo, R.; Oshimura, N.; Kuwata, N.; Kawamura, J., Degradation Mechanism of LiNi0.82Co0.15Al0.03O2 Positive Electrodes of a Lithium-Ion Battery by a Long-Term Cycling Test. *J Electrochem Soc* **2014,** *161* (6), A1007-A1011.
5. Sallis, S.; Pereira, N.; Mukherjee, P.; Quackenbush, N. F.; Faenza, N.; Schlueter, C.; Lee, T. L.; Yang, W. L.; Cosandey, F.; Amatucci, G. G.; Piper, L. F. J., Surface degradation of Li1-xNi0.80Co0.15Al0.05O2 cathodes: Correlating charge transfer impedance with surface phase transformations. *Appl Phys Lett* **2016,** *108* (26).
6. Bianchini, M.; Roca-Ayats, M.; Hartmann, P.; Brezesinski, T.; Janek, J., There and Back Again-The Journey of LiNiO2 as a Cathode Active Material. *Angew Chem Int Edit* **2019,** *58* (31), 10434-10458.
7. Kong, F. T.; Liang, C. P.; Wang, L. H.; Zheng, Y. P.; Perananthan, S.; Longo, R. C.; Ferraris, J. P.; Kim, M.; Cho, K., Kinetic Stability of Bulk LiNiO2 and Surface Degradation by Oxygen Evolution in LiNiO2-Based Cathode Materials. *Adv Energy Mater* **2019,** *9* (2).
8. Abraham, D. P.; Twesten, R. D.; Balasubramanian, M.; Kropf, J.; Fischer, D.; McBreen, J.; Petrov, I.; Amine, K., Microscopy and spectroscopy of lithium nickel oxide-based particles used in high power lithium-ion cells. *J Electrochem Soc* **2003,** *150* (11), A1450-A1456.

9. Makimura, Y.; Zheng, S. J.; Ikuhara, Y.; Ukyo, Y., Microstructural Observation of LiNi0.8Co0.15Al0.05O2 after Charge and Discharge by Scanning Transmission Electron Microscopy. *J Electrochem Soc* **2012,** *159* (7), A1070-A1073.

10. Mukherjee, P.; Faenza, N. V.; Pereira, N.; Ciston, J.; Piper, L. F. J.; Amatucci, G. G.; Cosandey, F., Surface Structural and Chemical Evolution of Layered LiNi0.8Co0.15Al0.050O2 (NCA) under High Voltage and Elevated Temperature Conditions. *Chem Mater* **2018,** *30* (23), 8431-8445.

11. Zheng, S. J.; Huang, R.; Makimura, Y.; Ukyo, Y.; Fisher, C. A. J.; Hirayama, T.; Ikuhara, Y., Microstructural Changes in LiNi0.8Co0.15Al0.05O2 Positive Electrode Material during the First Cycle. *J Electrochem Soc* **2011,** *158* (4), A357-A362.

12. Hwang, S.; Chang, W.; Kim, S. M.; Su, D.; Kim, D. H.; Lee, J. Y.; Chung, K. Y.; Stach, E. A., Investigation of Changes in the Surface Structure of LixNi0.8Co0.15Al0.05O2 Cathode Materials Induced by the Initial Charge. *Chem Mater* **2014,** *26* (2), 1084-1092.

13. Lee, H.; Jo, E.; Chung, K. Y.; Byun, D.; Kim, S. M.; Chang, W., In-Depth TEM Investigation on Structural Inhomogeneity within a Primary LixNi0.835Co0.15Al0.015O2 Particle: Origin of Capacity Decay during High-Rate Discharge. *Angew Chem Int Edit* **2020,** *59* (6), 2385-2391.

14. Wu, L. J.; Nam, K. W.; Wang, X. J.; Zhou, Y. N.; Zheng, J. C.; Yang, X. Q.; Zhu, Y. M., Structural Origin of Overcharge-Induced Thermal Instability of Ni-Containing Layered-Cathodes for High-Energy-Density Lithium Batteries. *Chem Mater* **2011,** *23* (17), 3953-3960.

15. Zhang, H. L.; Karki, K.; Huang, Y. Q.; Whittingham, M. S.; Stach, E. A.; Zhou, G. W., Atomic Insight into the Layered/Spinel Phase Transformation in Charged LiNi0.80Co0.15Al0.05O2 Cathode Particles. *J Phys Chem C* **2017,** *121* (3), 1421-1430.

16. Gu, M.; Belharouak, I.; Zheng, J. M.; Wu, H. M.; Xiao, J.; Genc, A.; Amine, K.; Thevuthasan, S.; Baer, D. R.; Zhang, J. G.; Browning, N. D.; Liu, J.; Wang, C. M., Formation of the Spinel Phase in the Layered Composite Cathode Used in Li-Ion Batteries. *Acs Nano* **2013,** *7* (1), 760-767.

17. Liu, H. S.; Harris, K. J.; Jiang, M.; Wu, Y.; Goward, G. R.; Botton, G. A., Unraveling the Rapid Performance Decay of Layered High-Energy Cathodes: From Nanoscale Degradation to Drastic Bulk Evolution. *Acs Nano* **2018,** *12* (3), 2708-2718.

18. Yan, P. F.; Nie, A. M.; Zheng, J. M.; Zhou, Y. G.; Lu, D. P.; Zhang, X. F.; Xu, R.; Belharouak, I.; Zu, X. T.; Xiao, J.; Amine, K.; Liu, J.; Gao, F.; Shahbazian-Yassar, R.; Zhang, J. G.; Wang, C. M., Evolution of Lattice Structure and Chemical Composition of the Surface Reconstruction Layer in Li1.2Ni0.2Mn0.6O2 Cathode Material for Lithium Ion Batteries. *Nano Lett* **2015,** *15* (1), 514-522.

19. Pereira, N.; Matthias, C.; Bell, K.; Badway, F.; Plitz, I.; Al-Sharab, J.; Cosandey, F.; Shah, P.; Isaacs, N.; Amatucci, G. G., Stoichiometric, morphological, and electrochemical impact of the phase stability of LixCoO2. *J Electrochem Soc* **2005,** *152* (1), A114-A125.

20. Xiao, P. H.; Shi, T.; Huang, W. X.; Ceder, G., Understanding Surface Densified Phases in Ni-Rich Layered Compounds. *Acs Energy Lett* **2019,** *4* (4), 811-818.

21. Nam, K. W.; Bak, S. M.; Hu, E. Y.; Yu, X. Q.; Zhou, Y. N.; Wang, X. J.; Wu, L. J.; Zhu, Y. M.; Chung, K. Y.; Yang, X. Q., Combining In Situ Synchrotron X-Ray Diffraction and Absorption Techniques with Transmission Electron Microscopy to Study the Origin of Thermal Instability in Overcharged Cathode Materials for Lithium-Ion Batteries. *Adv Funct Mater* **2013,** *23* (8), 1047-1063.

22. Yoon, W. S.; Haas, O.; Muhammad, S.; Kim, H.; Lee, W.; Kim, D.; Fischer, D. A.; Jaye, C.; Yang, X. Q.; Balasubramanian, M.; Nam, K. W., In situ soft XAS study on nickel-based layered cathode material at elevated temperatures: A novel approach to study thermal stability. *Sci Rep-Uk* **2014,** *4*.

23. Dahn, J. R.; Fuller, E. W.; Obrovac, M.; Vonsacken, U., Thermal-Stability of Lixcoo2, Lixnio2 and Lambda-Mno2 and Consequences for the Safety of Li-Ion Cells. *Solid State Ionics* **1994,** *69* (3-4), 265-270.

24. Guilmard, M.; Croguennec, L.; Denux, D.; Delmas, C., Thermal stability of lithium nickel oxide derivatives. Part I: LixNi1.02O2 and LixNi0.89Al0.16O2 (x = 0.50 and 0.30). *Chem Mater* **2003,** *15* (23), 4476-4483.

25. Guilmard, M.; Croguennec, L.; Delmas, C., Thermal stability of lithium nickel oxide derivatives. Part II: LixNi0.70Co0.15Al0.15O2 and LixNi0.90Mn0.10O2 (x = 0.50 and 0.30). Comparison with LixNi1.02O2 and LixNi0.89Al0.16O2. *Chem Mater* **2003,** *15* (23), 4484-4493.

26. Das, H.; Urban, A.; Huang, W. X.; Ceder, G., First-Principles Simulation of the (Li-Ni-Vacancy)O Phase Diagram and Its Relevance for the Surface Phases in Ni-Rich Li-Ion Cathode Materials. *Chem Mater* **2017,** *29* (18), 7840-7851.

27. Faenza, N. V.; Pereira, N.; Halat, D. M.; Vinckeviciute, J.; Bruce, P.; Radin, M. D.; Mukherjee, P.; Badway, F.; Halajko, A.; Cosandey, F.; Grey, C. P.; Van der Ven, A.; Arnatucci, G. G., Phase Evolution and Degradation Modes of R(3)over-barm LixNi1-y-zCoyAlz,O-2 Electrodes Cycled Near Complete Delithiation. *Chem Mater* **2018,** *30* (21), 7545-7574.

28. Hartel, P.; Rose, H.; Dinges, C., Conditions and reasons for incoherent imaging in STEM. *Ultramicroscopy* **1996,** *63* (2), 93-114.

29. Pennycook, S. J., Z-Contrast Stem for Materials Science. *Ultramicroscopy* **1989,** *30* (1-2), 58-69.

30. Graetz, J.; Ahn, C. C.; Yazami, R.; Fultz, B., An electron energy-loss spectrometry study of charge compensation in LiNi0.8Co0.2O2. *J Phys Chem B* **2003,** *107* (13), 2887-2891.

31. Cosandey, F.; Su, D.; Sina, M.; Pereira, N.; Amatucci, G. G., Fe valence determination and Li elemental distribution in lithiated FeO0.7F1.3/C nanocomposite battery materials by electron energy loss spectroscopy (EELS). *Micron* **2012,** *43* (1), 22-29.

32. Mukherjee, P.; ; Lu, P.; ; Faenza, N.; ; Pereira, N.; ; Amatucci, G. G.; and; Cosandey, F., From Nanometer to Atomic Resolution X-ray EDS analysis of Al in Ni-rich Layered Oxide Li-Ion Cathodes. *Microscopy and Microanalysis* **2017,** *23* ((Suppl 1)), 386-387.

33. Zou, L. F.; Zhao, W. G.; Liu, Z. Y.; Jia, H. P.; Zheng, J. M.; Wang, G. F.; Yang, Y.; Zhang, J. G.; Wang, C. M., Revealing Cycling Rate-Dependent Structure Evolution in Ni-Rich Layered Cathode Materials. *Acs Energy Lett* **2018,** *3* (10), 2433-2440.

34. Li, L. Z.; Self, E.; Darbar, D.; Zou, L. F.; Bhattacharya, I.; Wang, D. H.; Nanda, J.; Wang, C. M., Hidden Subsurface Reconstruction and Its Atomic Origins in Layered Oxide Cathodes. *Nano Lett* **2020,** *20* (4), 2756-2762.

35. Tarascon, J. M.; Gozdz, A. S.; Schmutz, C.; Shokoohi, F.; Warren, P. C., Performance of Bellcore's plastic rechargeable Li-ion batteries. *Solid State Ionics* **1996,** *86-8*, 49-54.

36. Wang, Z. L.; Yin, J. S.; Jiang, Y. D., EELS analysis of cation valence states and oxygen vacancies in magnetic oxides. *Micron* **2000,** *31* (5), 571-580.

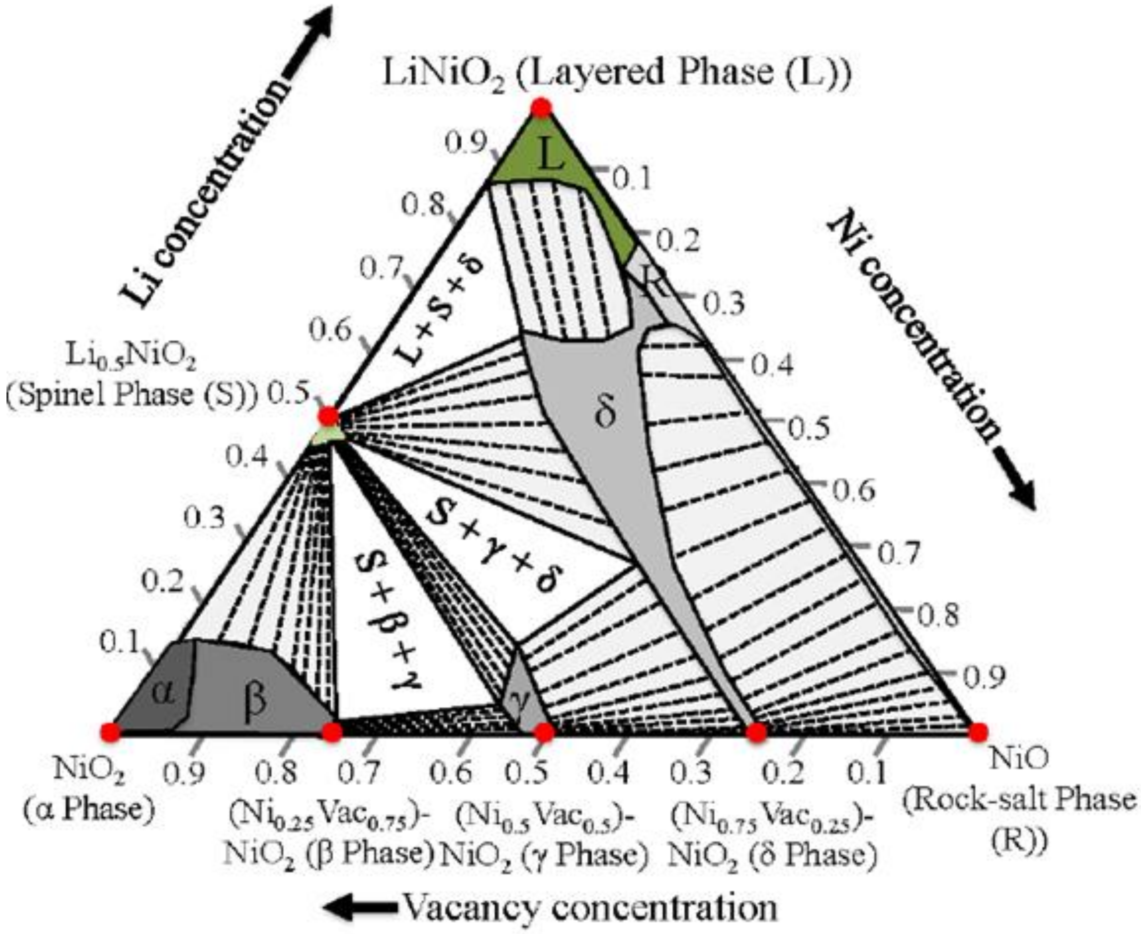

Figure 1: Calculated phase diagram of $LiNiO_2$. The phases of interest are in the base line of the triangle, which shows variation of phases from NiO to NiO_2 formed after differing levels of oxygen loss. Obtained with permission from ACS Chemistry of Materials **2017,** *29* (18), 7840-7851.

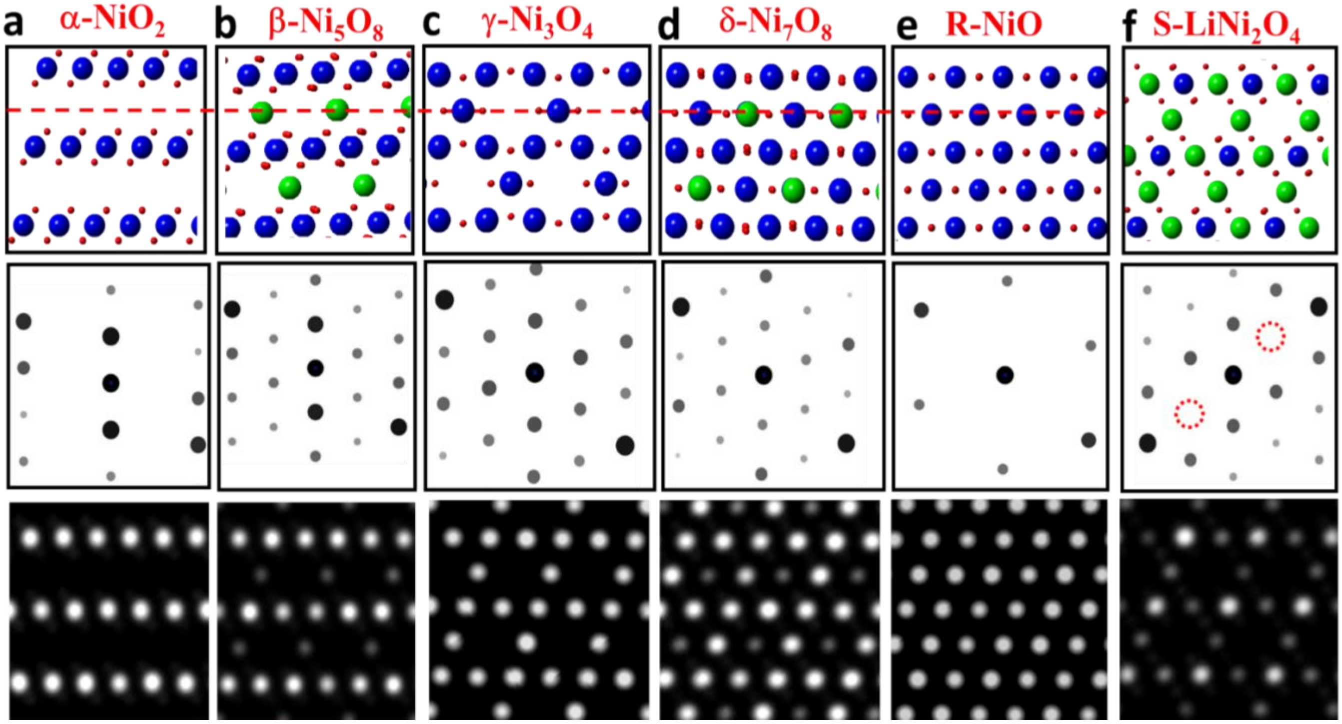

Figure 2: Top row (a-e): Projection of phases along the oxygen reduction axis of the phase diagram with O in red and Ni in blue/green. In this projection, the Ni sites are either empty, half full (green atomic column) or fully occupied (blue atomic column). The gradual periodic filling of the Li (3b) layer with Ni^{+2} cations is shown with a red dashed arrow. Middle row (a-e): The simulated selected area diffraction patterns of the phases mentioned in the top row. Bottom row (a-e): Simulated HAADF-STEM images of the above phases. Scattering from O and Li is too weak to be visible and only Ni show some contrast which is proportional to the number of Ni atoms along a specific atomic column. (f) The $LiNi_2O_4$ spinel phase is presented as a reference. The dashed circles in the spinel diffraction pattern show kinematically forbidden reflections. All these figures are viewed along the equivalents of the $[110]_L$ zone axis of the layered structure.

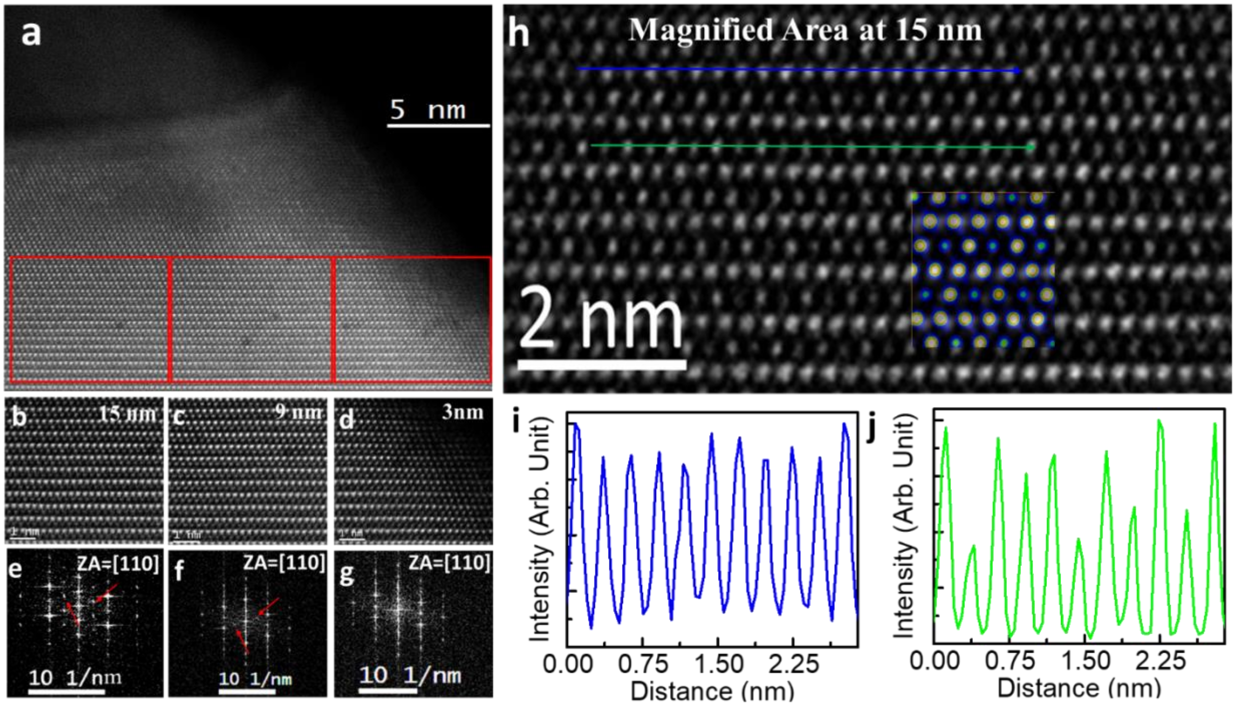

Figure 3: (a) HAADF STEM image of a LNO particle viewed along $[110]_L$. The magnified areas (b, c, d) show evolution of STEM contrast as a function of distance from the edge. (e, f, d) are their corresponding FFTs. The FFTs show emergence of extra spots marked by red arrows not belonging to parent trigonal phase. (h) Enlarged HAADF STEM image of the area of LNO ~ 15 nm from the edge. The simulated δ-$Ni_{1.75}O_2$ phase in overlaid on the experimental image. (i) Intensity profile along the blue line in the Ni layer is constant while in (j) the intensity profile along the green line in the Li layer revealing a periodic variation in contrast.

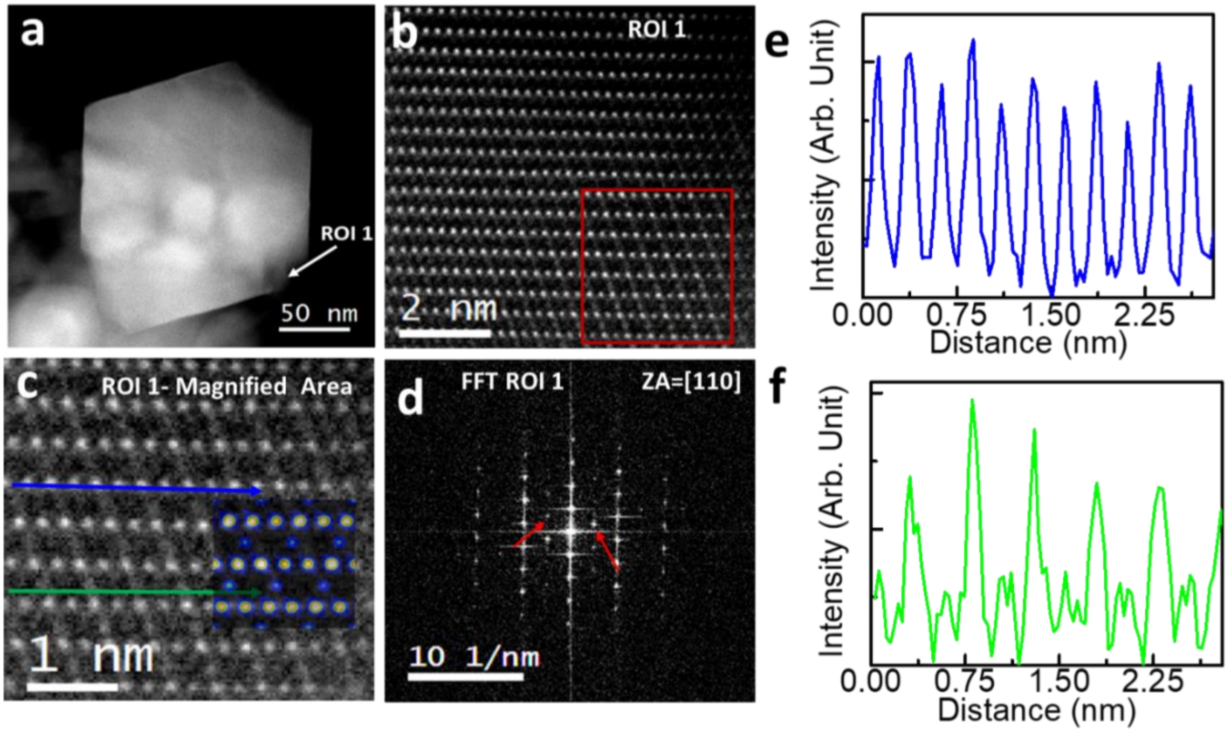

Figure 4: (a) HAADF STEM image of LNA particle viewed along $[110]_L$ with an enlarged image of ROI 1 shown in (b). The boxed area enlarged in (c) shows a STEM contrast where alternative Li sites are occupied by Ni ions. The simulated β-$Ni_{1.25}O_2$ phase in overlaid on the experimental image. (d) The corresponding FFT shows extra spots originating from this alternative occupancy at Li sites (marked with arrows). (e) Intensity profile along the blue line in the Ni layer shows a small variation in contrast. (f)The intensity profile along the green line in the Li layer reveals a doubling in contrast periodicity.

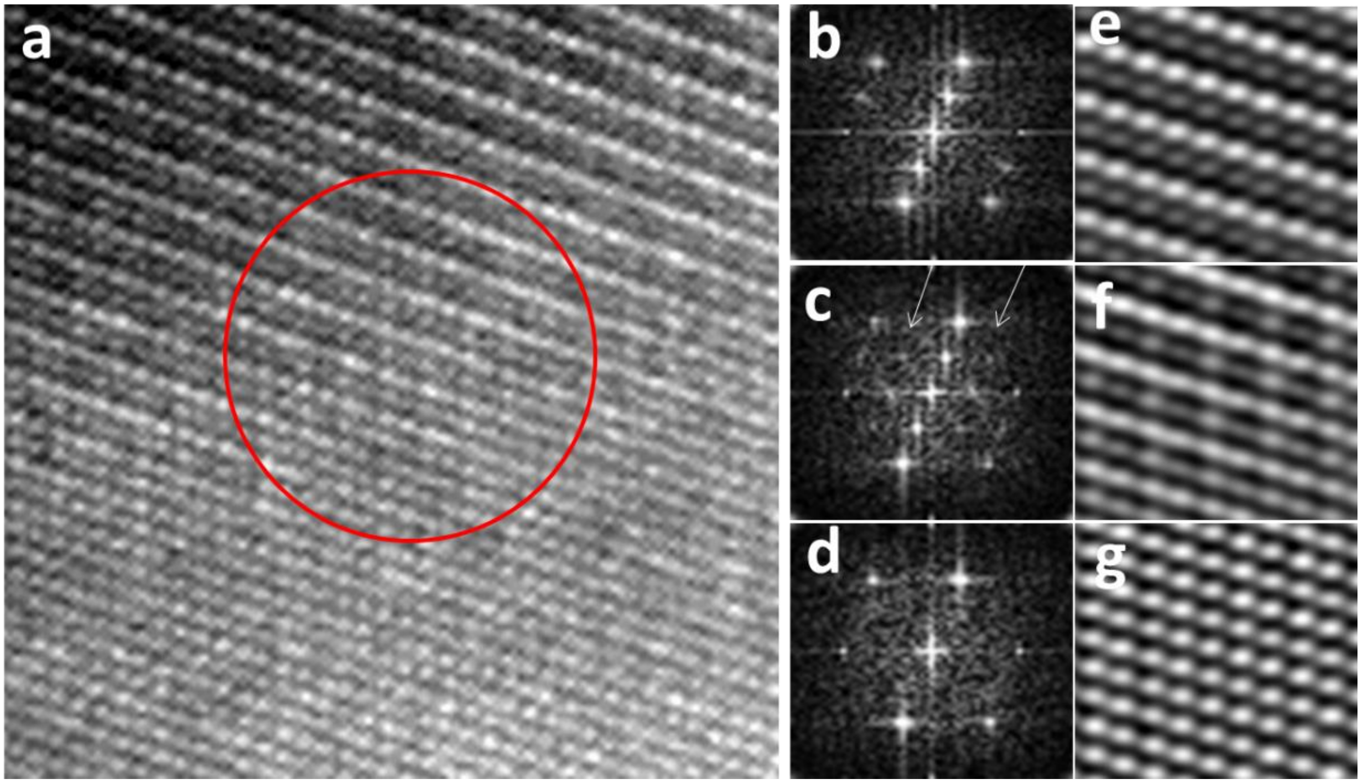

Figure 5: (a) HAADF STEM image of the interface area in LNA between layered and rocksalt phases. FFT form regions taken from (b) layered, (c) intermediate and (d) rocksalt. The intermediate FFT (c) shows the presence of extra reflections marked by arrows. The corresponding Fourier filtered images are shown in (e,f, g). The intermediate region reveals a periodic ordered contrast in the Li layer.